Macromolecular structure determination by cryo-electron microscopy

Helen R. Saibil

Department of Crystallography, Birkbeck College, Malet Street, London WC1E 7HX, England

Correspondence e-mail:
h.saibil@mail.cryst.bbk.ac.uk

Recent advances in transmission electron microscopy (EM) hardware, low-temperature methods and image-processing software have made cryo-EM an important complement to X-ray crystallography and NMR for macromolecular structure determination, particularly of large assemblies. This review provides a summary of the main advances and a survey of the capabilities of this approach.

## 1. Introduction: the role of cryo-EM in structural biology

Cryo-electron microscopy (cryo-EM) extends the capabilities of structural biology. In the three-dimensional (3D) structure determination of macromolecules, X-ray crystallography covers the full range from small molecules to very large assemblies such as viruses with molecular masses of megadaltons. The limiting factors are expression, crystallization and the stability and homogeneity of the structure. In the case of NMR, structures can be determined from isotopically labelled molecules in solution, but the size limit, although increasing, is presently of the order of 100 kDa. Dynamic aspects can be quantified, but again the structure of mixed species cannot be determined. Where does cryo-EM fit in? It provides complementary information to the other methods, being able to tackle very large assemblies and transient or mixed species, and usually requires small amounts of material. Although most of the structures so far determined are not at atomic resolution, cryo-EM information can be very effectively combined with partial atomic structure detail from the other methods to give new information on large complexes. It is also a powerful tool for studying conformational changes in large assemblies.

The wide range of possible EM sample geometries is shown in Fig. 1. EM structure analysis can be performed on samples ranging from highly ordered assemblies such as 2D crystals to asymmetric randomly oriented individual complexes (single particles), provided the particles are above a lower size limit (several hundred kDa). Different data-collection methods and processing software have been developed for the various sample geometries. In general, the more ordered assemblies have yielded the highest resolution maps, since they present the largest number of repeats of the asymmetric unit in well defined positions and orientations. However, the single-particle methods are beginning to catch up in the resolution achievable and they offer the advantage that crystallization is not required.

2. Electron optics and image formation

For a text and review on this subject see, for example, Hawkes & Valdrè (1990) and Wade (1992). Cryo-EM provides 3D electron-scattering density maps of macromolecules which are very similar to the electron-density maps determined by X-ray crystallography. Structure information is obtained from the elastic scattering; the accompanying inelastic scattering causes radiation damage. Scattering events with 1.5 Å X-rays are 1000 times more damaging than those with 0.025 Å electrons, but the cross-section for electron scattering is 10^5 times greater. Therefore, radiation damage is a much more serious problem for EM and cryo-cooling is essential for imaging of high-resolution detail. Because of the large scattering cross-section, the sample must be very thin (<2000 Å) to avoid multiple scattering. Radiation damage is still limiting even at low temperature. Therefore, the image exposures are the weakest possible to obtain a measurable signal and the signal-to-noise ratio of the recorded images is extremely low.

Thin samples of biological molecules fulfil the weak phase approximation, the theory of image formation which is used to describe and analyse the phase-contrast images of weakly scattering specimens. Although there is no contrast when the image is in focus, spherical aberration and defocus combine to give a phase-contrast image. The imaging characteristics are described by the contrast-transfer function (CTF), which can be derived from the weak phase approximation. The CTF describes the contrast transfer as a function of spatial frequency. It has alternating bands of positive and negative contrast, seen in the scattering from carbon film as Thon rings. Its real-space equivalent is the point-spread function, the
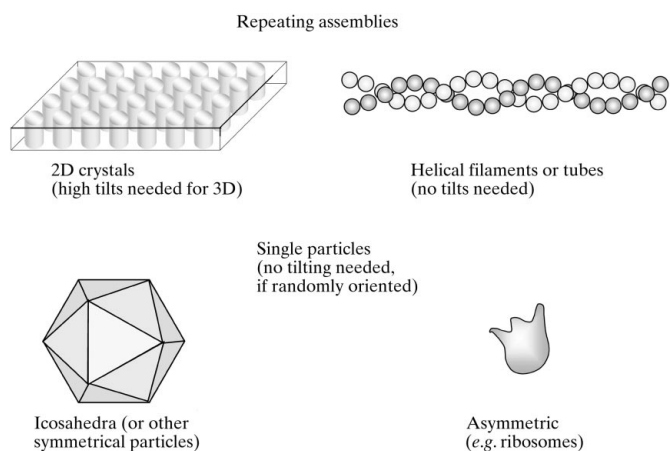
Figure 1
EM sample geometry. A variety of macromolecular assemblies, both ordered and as individual complexes, can be analysed by cryo-EM. Of the ordered assemblies, the 2D crystals are the ones which have yielded atomic resolution structures. However, they must be tilted to high angles to provide 3D data. The helical assemblies are only crystalline in one dimension and the varying orientation of the subunit around the helical axis is useful in providing a set of different views. No crystallization or naturally occurring order is necessary in the case of single particles (isolated complexes in solution), provided they are large enough to be detected and analysed. Single particles can range from highly symmetric, such as the icosahedral viruses, to asymmetric structures, such as the ribosome.

microscope image of a small point object. In order to restore the correct structural information, the images must be corrected for the CTF. Images must be collected at a range of defocus values to fill in missing data from each, caused by zeros in the CTF whose positions vary with the defocus.

The electron optical resolution of transmission EM is around 1 Å, much coarser than the diffraction limit imposed by the electron wavelength of ∼0.025 Å. The resolution is restricted by the small aperture size needed because of aberrations in the electromagnetic lenses. Small apertures give a large depth of field, which has important consequences for 3D reconstruction which are discussed below. For radiation-insensitive conductive samples, high resolution can be achieved. Difficulties for macromolecules are radiation sensitivity, specimen movement in the electron beam (especially at high tilt angles) and low contrast. These effects have so far limited the resolution of macromolecular imaging to ∼3 Å in the best cases. Particularly for single particles, the loss of contrast beyond ∼20 Å resolution is a major limitation. This limit can be greatly extended by the use of a field emission gun (FEG) electron source. The small apparent source size gives a highly coherent illumination that provides much better phase contrast at high resolution. Higher accelerating voltages (200–300 kV instead of the routine 100–120 kV) also provide resolution advantages.
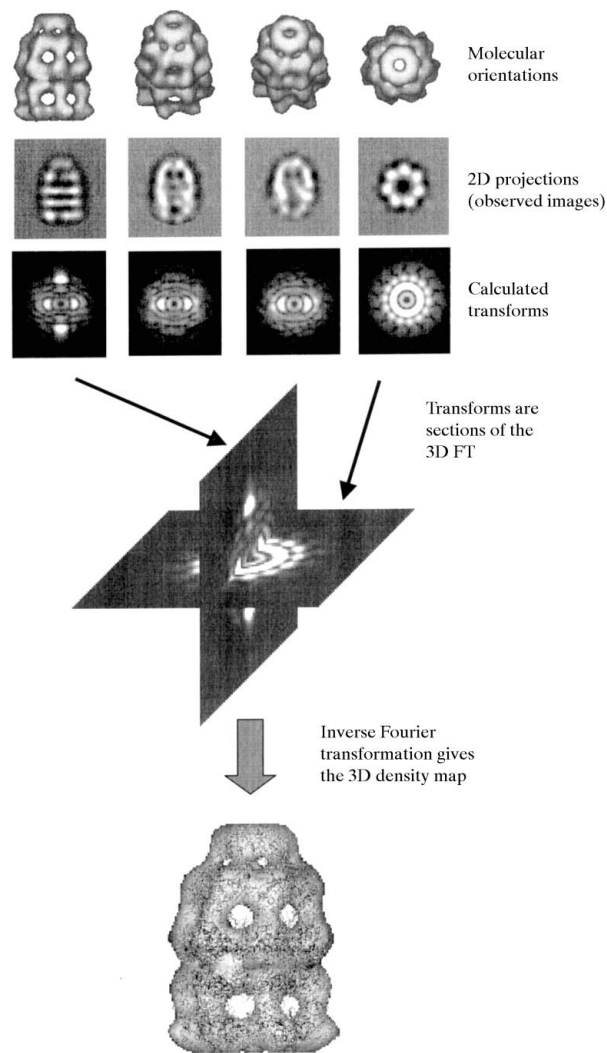
A consequence of the large depth of field is that the observed image is a 2D projection of the 3D density, which can be recovered from a set of projections from different view directions by tomographic reconstruction. Reconstruction from projections was invented for EM (DeRosier & Klug, 1968; Crowther et al., 1970) and then taken up for computer tomography scanning in medicine. Fig. 2 shows the principle of Fourier reconstruction from projections. For thick specimens (≥2000 Å), the projection assumption is not valid and there is a focus gradient through the specimen (equivalent to non-flatness of the Ewald sphere). This problem is alleviated at higher voltages, which increase the depth of field. Software is still being developed for correction of the focus gradient, which will be significant for high-resolution analysis of thicker specimens.

The relation between imaging and diffraction is shown schematically in Fig. 3. The microscope can be used either as an imaging or a diffraction instrument. Unlike diffraction experiments, in which phase information is lost, the image recorded by microscopy contains both amplitude and phase information. However, a much higher electron dose is needed to record the image than for the electron-diffraction pattern. Mechanical stability is particularly critical for obtaining phases. Movement does not affect the amplitudes in electron diffraction provided the crystalline area stays in the beam, but any movement during image recording ruins the image.

3. Cryo methods

The development of cryo-EM has been a major technical advance for two reasons: the low temperature of the specimen slows radiation damage and, even more importantly, the
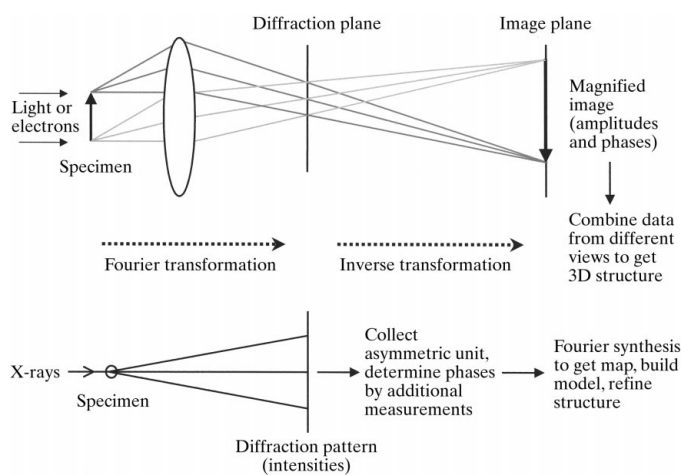
native hydrated macromolecular structure is preserved in the microscope vacuum by vitrification. A more routine method for imaging macromolecular complexes is negative-stain EM, in which the complex is dried down in a pool of heavy-metal stain. The method is simple and provides high contrast, but only the overall shape is revealed by negative contrast and the native structure may be distorted by dehydration. Fig. 4 is a schematic diagram of a negatively stained and a cryo-EM sample. With the frozen hydrated specimen, the native struc-

ture is maintained and internal detail is recorded, although with very low contrast. The vitrification method (Dubochet *et al.*, 1988) is shown schematically in Fig. 5. A drop of solution on the grid is blotted with filter paper to leave a very thin layer (1–2000 Å) just before plunging into a coolant with high heat conductivity, usually liquid ethane. Since the layer is so thin, the water is vitrified into a solid glass-like state and no ice crystals form. Because the vitrification step is very rapid (freezing takes place in <<1 msec), it is possible to capture very short-lived structural states by spraying a ligand, or flashing light in the case of photosensitive specimens, onto the grid just before it plunges into the ethane. The spray method was developed by Berriman & Unwin (1994) for capturing the acetylcholine-activated state of the nicotinic acetylcholine receptor, which has a lifetime of only 10 msec. A stopped-flow mixer system combined with an atomizer spray has been developed for actomyosin kinetic studies by White *et al.* (1998).

The vitrified grid is transferred into the microscope using a special cryotransfer holder to maintain the low temperature and minimize ice contamination of the surface. The state of the water layer can be assessed by electron diffraction. Of major concern for ice samples is the mechanical stability of the frozen specimen in the electron beam. Specimen stability, particularly at high tilt, is improved in state-of-the-art microscopes with fixed specimen cartridges not coupled to the external warm goniometer rod. Beam-induced specimen charging is also a problem for ice specimens. The examples of atomic resolution so far obtained by cryo-EM have been achieved with 2D crystals on solid carbon support films. However, to optimize contrast, single-particle cryo-EM is typically performed on perforated carbon films so that regions of ice unsupported by carbon film are imaged. Unsupported

Figure 2
The principle of 3D reconstruction from 2D projections. A set of four different molecular orientations, displayed as rendered iso-surfaces, are shown above their corresponding 2D projections. Real cryo-EM images are very noisy versions of these projections. The Fourier transform of each projection, shown below the projections, is a section through the 3D Fourier transform of the structure (DeRosier & Klug, 1968). The 3D transform is represented by two intersecting transform sections, derived from the side and end views of the structure. Once enough sections are available, the full 3D transform can be interpolated and inverse transformed into a 3D density map. The map is shown with the backbone of the structure to emphasize the fact that the full 3D density is obtained, including internal features. Surface rendering is generally used to represent such maps when the resolution is insufficient to provide an atomic model of the structure.
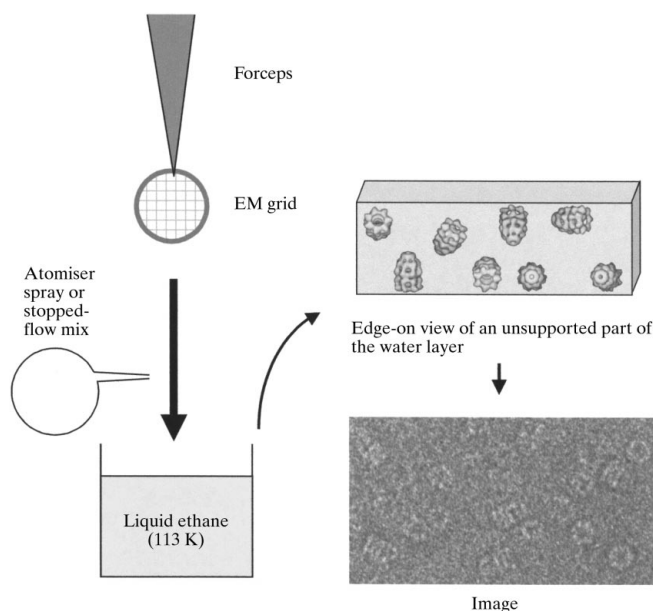

Figure 3
The relationship between imaging and diffraction. A simplified schematic view of imaging and diffraction shows that the waves scattered by the specimen form a Fourier transform, observed as a diffraction pattern. The objective lens in a microscope recombines the scattered waves in an inverse transformation, forming the magnified image. In the diffraction experiment, only the diffracted intensities are recorded and the lost phase information must be retrieved by other methods.

research papers

ice has lower conductivity than carbon film. The contrast is more critical for single particles than for ordered assemblies, since the position and orientation must be determined for each particle individually.

There has been much recent development in the area of single-particle image-processing methods and similar ideas are also being used for disorder correction of subunits or groups of subunits in ordered assemblies. The different sample geometries require different data-collection and processing approaches. These are described in the following sections.
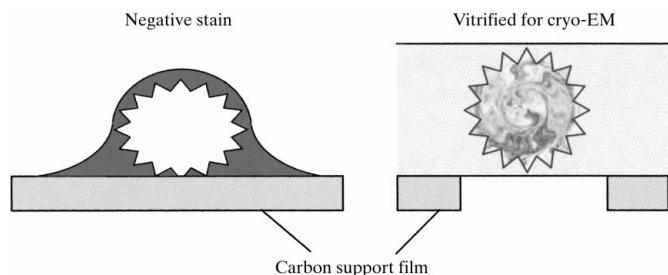
Figure 4
Negative-stain and cryo-EM. A virus particle on a carbon support film is shown in schematic side view. The particle is outlined with good contrast by heavy-metal stain, but is somewhat flattened by the accompanying dehydration. It is preserved in the native hydrated state in the cryo-sample but the protein–ice contrast is very low. In order to maximize the contrast, the cryo-specimen is imaged over holes in the carbon support film.
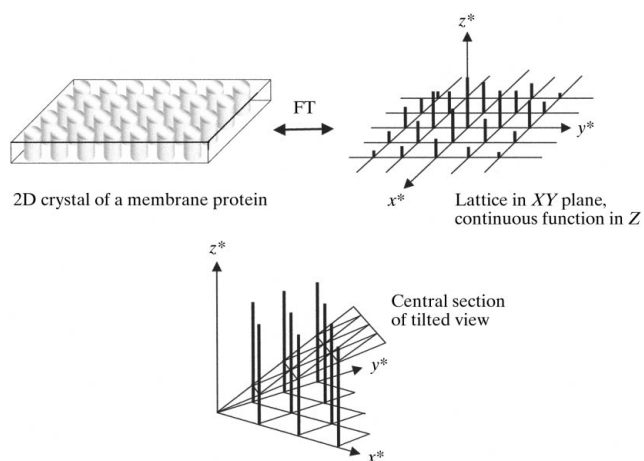

Figure 5
Vitrification of cryo-EM specimens and time-resolved cryo-EM. A cryo-EM grid with a thin film of solution is plunged into liquid ethane for vitrification. Time-resolved experiments are possible by spraying a reagent onto the grid just before it enters the ethane, using an atomiser. A time resolution of several milliseconds can be achieved. To the right is a schematic view of a part of the frozen water layer, with macromolecules trapped in different orientations. Bottom right, part of a cryo-EM image showing weak and noisy views of the complexes.

4. 2D crystals

Cryo-EM reconstructions of 2D crystals have yielded high-resolution maps (3–4 Å) of sufficient quality to define most of the protein conformation in the case of bacteriorhopsin (Henderson *et al.*, 1990), plant light-harvesting protein (Kühlbrandt *et al.*, 1994) and tubulin (Nogales *et al.*, 1998). In these studies, the crystals were partially dried down in sugar or tannin solutions and observed at low temperature. Not all 2D crystals can be treated in this way and the resulting loss of low-resolution contrast is incompatible with single-particle studies.

Large 2D crystals are most favourable for collecting a large number (∼10^6 copies) of images of the asymmetric unit. However, a drawback for 3D reconstruction is the need to collect the different angular views. There is a missing cone of data because the maximum tilt angle possible is ∼60°. Moreover, the collection and processing of high tilt angle images is much more difficult than for untilted images. The missing data results in anisotropic resolution. Poorer resolution normal to the image plane means that features in the map along that direction will lose definition. For example, the loops joining transmembrane helices are not usually seen. A diagram of a 2D crystal and the transform geometry is shown in Fig. 6. With large-area crystals, accurate amplitudes can be obtained by electron diffraction and combined with the phases measured from the images. So far, structure determination by this method has been slow, but it may be the only route for difficult samples such as membrane proteins. In addition to the direct measurement of phases that distinguishes microscopy from crystallography, the images can be corrected for short-range lattice disorder. A computational procedure termed 'unbending' is used to straighten out deviations from a perfect lattice (Fig. 7). A small region of the lattice, or else a reprojection of an initial 3D map, is cross correlated with the whole
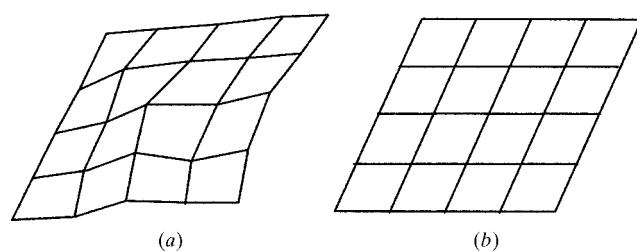

Figure 6
Data-collection geometry for 2D crystals. Each lattice line will have a continuously varying amplitude and phase along its Z coordinate. The tilted views sample the lattice lines at different heights in Fourier space. Most of the 3D FT can be determined by combining these sections derived from different tilt views in projection. However, in EM of 2D crystals there is a missing cone of information because the maximum tilt angle of the crystal is limited to about 60°. Figure adapted from Amos *et al.* (1982).

crystal image and the peaks are mapped out and compared with the positions expected for a perfect lattice (Henderson *et al.*, 1990; Kunji *et al.*, 2000). Regions of the crystal image deviating from perfect lattice points are shifted and interpolated into the idealized lattice. This extends the resolution of the calculated transform section from each image. Lattice reflections calculated from each image are assembled into the 3D transform, which is interpolated and inverse transformed to give the 3D density map. One aspect that has been quantified by comparison of electron diffraction and diffraction amplitudes calculated from lattice images is the severe fall-off of signal at high resolution (Fig. 8). This amplitude loss makes it necessary to collect 10–100 times more data than theoretically necessary to achieve high resolution. It is thought to arise from a combination of sample, electron-optical, mechanical and processing defects.

5. Helical assemblies

Many biological assemblies occur naturally in helical form, particularly cytoskeleton filaments and nucleic acid structures. Helical crystallization has also been used for structure determination, particularly in the case of membrane proteins, which can be induced to form tubular crystals. Helices are 1D crystals. Diffraction from a helix occurs on a set of layer lines related to the pitch repeat (Fig. 9). An advantage of helical analysis over 2D crystals is that the asymmetric unit is presented over a range of angular views and tilting is not usually necessary for 3D reconstruction (DeRosier & Moore, 1970). However, it is more difficult to collect 10^6 copies of the asymmetric unit and achieve high resolution. Disorder corrections are more complicated (Beroukhim & Unwin, 1997), but 4–5 Å resolution has been achieved with tubular crystals of the nicotinic acetylcholine receptor (Miyazawa *et al.*, 1999). A remarkable recent result is the direct visualization of β-sheet structure in an amyloid fibril (Serpell & Smith, 2000). In that case, the β-strands appear to be in precise register in several β-sheets, giving sufficient contrast for the 4.8 Å repeat to be seen in raw images of well oriented fibrils.
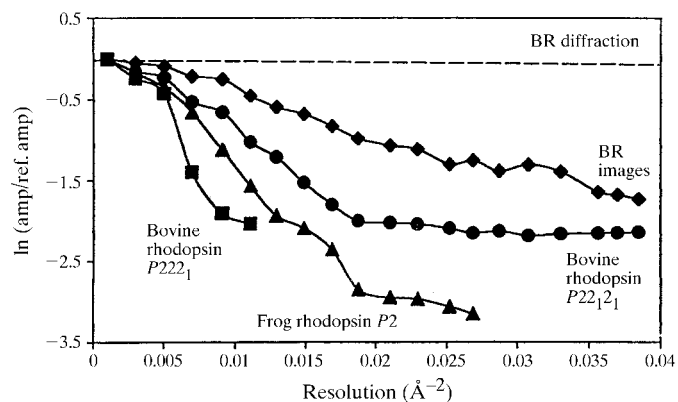
6. Single-particle analysis

Ordered assemblies can be dispensed with altogether if an isolated complex is large enough (a few hundred kDa) to give sufficient signal to locate it in a noisy low-contrast image and then to determine its orientation with sufficient accuracy. There have been great advances recently in the application of single-particle methods to macromolecular complexes. For a text on this subject see Frank (1996). The early ideas were developed before cryo-EM using negatively stained samples. An initial alignment can be performed by cross correlation of all the images with their rotationally symmetrized average. With a few iterations this brings them all to the same centre. With a large enough data set to give good statistics (a few thousand images) multivariate statistical analysis (MSA; Fig. 10) can be used to sort similar images into subsets; class averages provide a significant improvement in the signal-to-noise ratio (van Heel & Frank, 1981; Frank, 1990). Class averages can reveal important orientation and/or biochemical variations present in a data set. Orientation analysis is much more straightforward if the sample is biochemically homogeneous.

There are two approaches to obtaining a first 3D model (a starting model for refinement): conical tilting or the use of common-line projections. If the particle exhibits a preferred orientation on the EM grid, a pair of images collected at high tilt ($60°$) and $0°$ tilt can be used to obtain a set of views of known orientation around a cone of angles (Radermacher *et al.*, 1987). This provides the hand, but causes some distortion because of the missing cone of $60–90°$ orientations and the poorer quality of high-tilt images. The other approach is to find the common lines between pairs of images, which are different projections of the same 3D structure. Once the signal-to-noise ratio has been improved by grouping similar images into class averages, all possible line projections can be compared between pairs of images to obtain their relative orientations (van Heel, 1987). This procedure, angular reconstitution, is used to obtain a set of initial angle assignments that generate a first 3D model. A related reciprocal-

Figure 7
Unbending. (*a*) A perfect 2D lattice would have a unit cell at each lattice point. In practice, macromolecules in images of 2D crystals are imperfectly ordered. The lattice disorder in (*b*) is exaggerated, but small distortions can be found by cross-correlation and corrected by non-linear interpolation of the image. Disorder correction greatly improves the resolution obtainable from such samples.
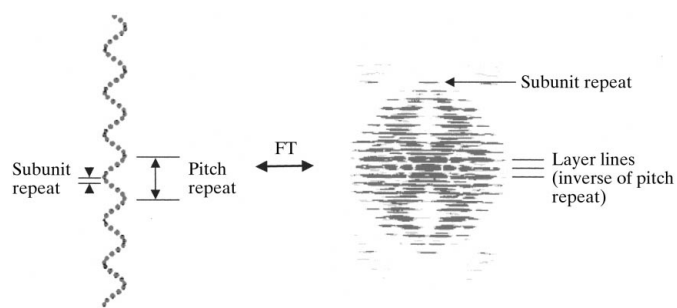

Figure 8
Amplitude loss from EM images as a function of resolution. Relative to the electron diffraction from bacteriorhodopsin (BR), the average amplitude calculated from images of various 2D crystals drops steadily with increasing resolution. This figure is reproduced from Krebs *et al.* (1998) by permission of Academic Press.
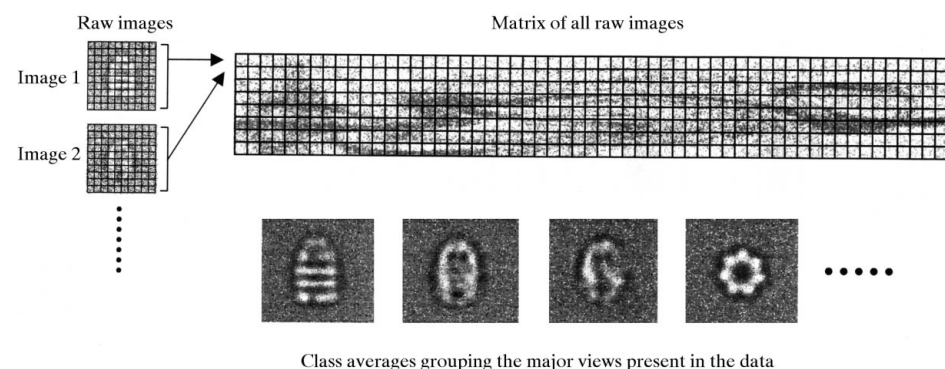
space approach has been well developed for the case of icosahedral symmetry, in which orientations are determined by searching for symmetry-related lines in transforms of individual particles or between particles (Crowther, 1971; Fuller *et al.*, 1996; Baker *et al.*, 1999). The common-lines approach has the advantage of not requiring any tilted images, but does not provide the absolute hand of the structure.

6.1. Orientation refinement

With a starting model from either approach or from a similar structure, in a low-resolution version of molecular replacement, the structure can be refined by projection matching (Harauz & Ottensmeyer, 1984; Penczek *et al.*, 1994; Baker & Cheng, 1996). The 3D model is reprojected into all directions, with an angular step determined by the resolution, the size of the object and the size of the data set. Considering

Figure 9
Helical diffraction. A helix can be considered as a 1D crystal, since it has a repeating structure along the axis giving rise to a set of layer lines in the diffraction pattern. If the symmetry of the helix is known, a full 3D reconstruction can be calculated from the untilted filament transform, since the subunit is imaged at different angles about the filament axis. The example shown is for the case of a helix with an integral number of subunits per helical pitch repeat.

the planes of transform sections diverging with resolution, a simple rule of thumb is given by $n = \pi D/R$, where n is the number of view orientations, D is the object diameter and R is the resolution (Crowther *et al.*, 1970). The set of raw images is cross-correlated with the whole set of projections to refine the position and orientation parameters (Fig. 11). At this stage, projections from more than one structure can be introduced in order to separate images in the data set into groups corresponding to different components of a mixture (see, for example, Schoehn *et al.*, 2000). The new set of image parameters is used to generate an improved 3D map and the process is iterated until the assignments converge. Convergence can be judged by the correlation between input and reprojected images, and by the stability of angle assignments over successive iterations. In the angular reconstitution procedure, the angle assignment is performed using class averages determined from MSA rather than raw images, because of their higher signal-to-noise ratio (see Orlova, 2000).
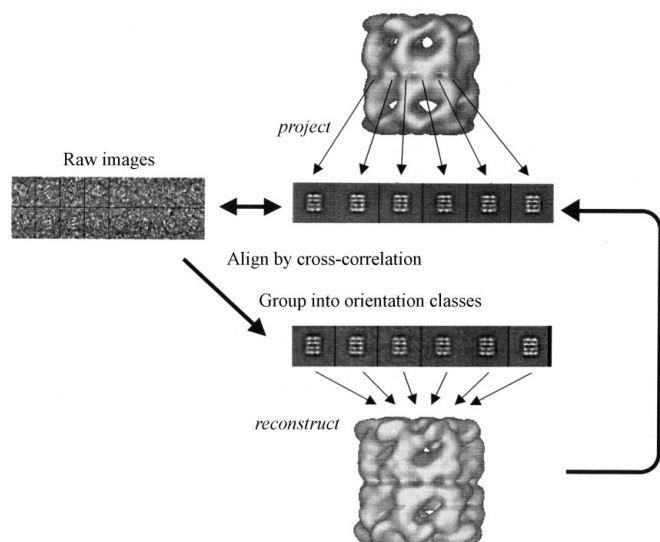
In principle, a sufficiently large set of single-particle images, if taken on a high-contrast/high-resolution microscope, can produce a 3 Å density map (Henderson, 1995). The most difficult case is for an asymmetric particle, such as the ribosome, which has stimulated development of the single-particle software systems *SPIDER* and *IMAGIC* (Frank *et al.*, 1996; van Heel *et al.*, 1996). A reciprocal-space approach to refinement is taken in the program *FREALIGN*, which minimizes the phase residual for each particle transform relative to the transform of the current 3D reconstruction (Grigorieff, 1998).

The most favourable single particles are those with high symmetry, such as icosahedral viruses. So far, the highest resolution single-particle analysis has been of the hepatitis B core particle, with a resolution of 7.4 Å (Böttcher *et al.*, 1997). Since cryo-EM of 2D crystals has led to 3 Å structures, it seems possible that a similar number of asymmetric units as single particles could also generate such a map, if movement in the ice and alignment accuracy are not limiting. Searching alignments by cross correlation is the most computationally intensive step in single-particle analysis and at present a target of 10^6 single-particle images for a 3 Å structure is limited by computing power. Moreover, it is still to be demonstrated that the orientation refinement and optical corrections can be performed with sufficient accuracy to obtain atomic resolution from single-particle images.
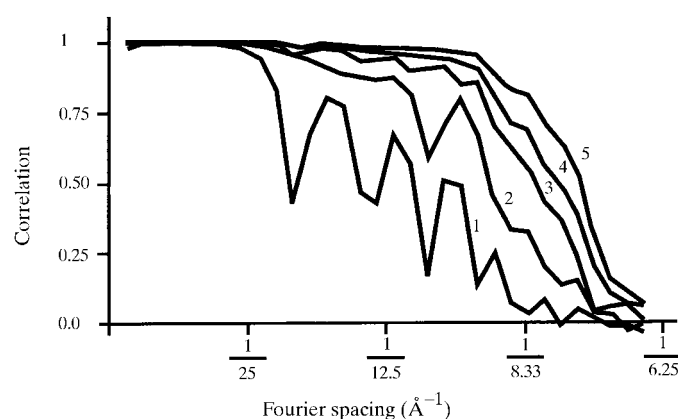

Figure 10
Image classification by multivariate statistical analysis. A large set of images is aligned to a common centre and then assembled into a matrix in which each row contains all the pixel values of a single image. Each raw image forms a row of the matrix. The first two images of a series and a small part of the matrix are shown. The eigenvectors of this matrix are difference images that represent the principal components of variation in the data set. Each image can then be represented by the average image ± a series of difference components. Similar images are classified into subgroups on the basis of the coefficients of these components. Similar average of each subgroup gives an image with a greatly improved signal-to-noise ratio.

6.2. Resolution assessment

Assessment of the map resolution from single-particle analysis is not entirely straightforward. A standard

method is to split the data set into two and to compare the Fourier terms of the two halves in resolution shells. This generates a plot known as the Fourier shell correlation and one criterion is to take the resolution value at which this curve has dropped to half its maximum value. A more optimistic criterion is to take the value at which the curve crosses a baseline curve for a random correlation with the appropriate

symmetry. An example set of Fourier shell correlations for different numbers of images is shown in Fig. 12. If the atomic structure is known, it is also possible to perform a Fourier shell correlation between the full EM data set and a map generated from the atomic coordinates. However, the Fourier shell correlation measurement is not always in agreement with comparisons between EM maps and crystal structures filtered to different resolutions. Grigorieff (2000) discusses statistical sources of inaccuracy in the Fourier shell correlations.

7. Conclusions: interpretation of cryo-EM maps

Considerable biological information, especially concerning conformational changes, can be obtained from cryo-EM studies. An extremely effective approach is to combine low-resolution maps of large complexes with atomic structures of individual components. Comparisons of different functional states such as intermediates in an ATPase cycle can also be very informative (for example, Roseman *et al.*, 1996). There are several ongoing efforts to improve docking and fitting procedures and this is discussed by other contributors to this issue. Looking to the even larger scale, cryo-EM studies, for example by tomography of organelles, small cells or tissue sections, can provide a bridge between cell biological function and molecular mechanisms.

Figure 11
Refinement by projection matching. A 3D map is projected into a set of different orientations to create reference images. Each raw image in the data set is translationally and rotationally aligned to each reference image in turn and is assigned the orientation of the one giving the highest correlation coefficient. The aligned images are grouped and averaged and these averages are used to create an improved 3D map. The procedure is iterated until the maps converge. Reprojections of the maps are compared to the preceding set of class averages to check for consistency.

Figure 12
Fourier shell correlations for hepatitis B core particles. Correlation plots are shown for data sets containing the following numbers of particles: 200 (curve 1), 1000 (2), 3000 (3), 6384 (4) and 6384 with full icosahedral symmetry imposed (5). Curve 1 was obtained from a single micrograph and the minima arise from frequencies with poor signal owing to CTF losses. When micrographs at different defocus values are combined, the minima are filled in because the zeros occur at different frequencies. This figure is reproduced from Böttcher *et al.* (1997) by permission of Macmillan Publishers Ltd.

References

Amos, L. A., Henderson, R. & Unwin, P. N. T. (1982). *Prog. Biophys. Mol. Biol.* **39**, 183–231.
Baker, T. S. & Cheng, R. H. (1996) *J. Struct. Biol.* **116**, 120–130.
Baker, T. S., Olson, N. H. & Fuller, S. D. (1999). *Microbiol. Mol. Biol. Rev.* **63**, 862–922.
Beroukhim, R. & Unwin, N. (1997). *Ultramicroscopy*, **70**, 57–81.
Berriman, J. & Unwin, N. (1994). *Ultramicroscopy*, **56**, 241–252.
Böttcher, B., Wynne, S. A. & Crowther, R. A. (1997). *Nature (London)*, **386**, 88–91.
Crowther, R. A. (1971). *Philos. Trans. R. Soc. London*, **261**, 221–230.
Crowther, R. A., DeRosier, D. J. & Klug, A. (1970). *Proc. R. Soc. London Ser. A*, **317**, 319–340.
DeRosier, D. J. & Klug, A. (1968). *Nature (London)*, **217**, 130–134.
DeRosier, D. J. & Moore, P. B. (1970). *J. Mol. Biol.* **52**, 355–369.
Dubochet, J., Adrian, M., Chang, J. J., Homo, J. C., Lepault, J., McDowell, A. W. & Schultz, P. (1988). *Quart. Rev. Biophys.* **21**, 129–228.
Frank, J. (1990). *Quart. Rev. Biophys.* **23**, 281–329.
Frank, J. (1996). *Three-Dimensional Electron Microscopy of Macromolecular Assemblies.* San Diego: Academic Press.
Frank, J., Radermacher, M., Penczek, P., Zhu, J., Li, Y., Ladjadj, M. & Leith, A. (1996). *J. Struct. Biol.* **116**, 190–199.
Fuller, S. D., Butcher, S. J., Cheng, R. H. & Baker, T. S. (1996). *J. Struct. Biol.* **116**, 48–55.
Grigorieff, N. (1998). *J. Mol. Biol.* **277**, 1033–1046.
Grigorieff, N. (2000). *Acta Cryst.* D**56**, 1270–1277.
Harauz, G. & Ottensmeyer, F. P. (1984). *Ultramicroscopy*, **12**, 309–320.
Hawkes, P. W. & Valdrè, U. (1990). *Biophysical Electron Microscopy.* London: Academic Press.

Heel, M. van (1987). *Ultramicroscopy*, **21**, 95–100; 111–124.

Heel, M. van & Frank, J. (1981). *Ultramicroscopy*, **6**, 187–194.

Heel, M. van, Harauz, G., Orlova, E., Schmidt, R. & Schatz, M. (1996). *J. Struct. Biol.* **116**, 17–24.

Henderson, R. (1995). *Quart. Rev. Biophys.* **28**, 171–193.

Henderson, R., Baldwin, J. M., Ceska, T. A., Zemlin, F., Beckmann, E. & Downing, K. H. (1990). *J. Mol. Biol.* **213**, 899–929.

Krebs, A., Villa, C., Edwards, P. C. & Schertler, G. F. X. (1998). *J. Mol. Biol.* **282**, 991–1003.

Kühlbrandt, W., Wang, D. N. & Fujiyoshi, Y. (1994). *Nature (London)*, **367**, 614–621.

Kunji, E. R. S., von Grunau, S., Oesterhelt, D. & Henderson, R. (2000). *Proc. Natl Acad. Sci. USA*, **97**, 4637–4642.

Miyazawa, A., Fujiyoshi, Y., Stowell, M. & Unwin, N. (1999). *J. Mol. Biol.* **288**, 765–786.

Nogales, E., Wolf, S. G. & Downing, K. H. (1998). *Nature (London)*, **391**, 199–203.

Orlova, E. V. (2000). *Acta Cryst.* D**56**, 1253–1258.

Penczek, P. A., Grassucci, R. A. & Frank, J. (1994). *Ultramicroscopy*, **53**, 251–270.

Radermacher, M., Wagenknecht, T., Verschoor, A. & Frank, J. (1987). *J. Microsc.* **146**, 113–136.

Roseman, A. M., Chen, S., White, H., Braig, K. & Saibil, H. R. (1996). *Cell*, **87**, 241–251.

Schoehn, G., Quaite-Randall, E., Jiménez, J. L., Joachimiak, A. & Saibil, H. R. (2000). *J. Mol. Biol.* **296**, 813–819.

Serpell, L. C. & Smith, J. M. (2000). *J. Mol. Biol.* **299**, 225–231.

Wade, R. H. (1992). *Ultramicroscopy*, **46**, 145–156.

White, H. D., Walker, M. L. & Trinick, J. (1998). *J. Struct. Biol.* **121**, 306–313.